

THE TIME-DEPENDENT WAVELET SPECTRUM OF HH 1 AND 2

A. C. Raga¹, B. Reipurth², A. Esquivel¹, D. González-Gómez³, and A. Riera^{4†}

Received June 15 2017; accepted January 26 2018

ABSTRACT

We have calculated the wavelet spectra of four epochs (spanning ≈ 20 yr) of H α and [S II] HST images of HH 1 and 2. From these spectra we calculated the distribution functions of the (angular) radii of the emission structures. We found that the size distributions have maxima (corresponding to the characteristic sizes of the observed structures) with radii that are logarithmically spaced with factors of $\approx 2 \rightarrow 3$ between the successive peaks. The positions of these peaks generally showed small shifts towards larger sizes as a function of time. This result indicates that the structures of HH 1 and 2 have a general expansion (seen at all scales), and/or are the result of a sequence of merging events resulting in the formation of knots with larger characteristic sizes.

RESUMEN

Hemos calculado el espectro de wavelet de cuatro épocas (cubriendo ≈ 20 años) de imágenes de H α y [S II] de HH 1 y 2 obtenidas con el HST. De estos espectros, calculamos funciones de distribución de los radios (angulares) de las estructuras emisoras. Encontramos que las distribuciones de tamaño tienen máximos (correspondientes a los tamaños característicos de las estructuras observadas) con radios espaciados logarítmicamente con factores de $\approx 2 \rightarrow 3$ entre picos sucesivos. Las posiciones de estos picos generalmente muestran pequeños corrimientos, hacia tamaños mayores en función del tiempo. Este resultado indica que las estructuras de HH 1 y 2 tienen una expansión (a todas las escalas) y/o son el resultado de una secuencia de eventos de fusión, que tiene como resultando la formación de nudos de mayores tamaños característicos.

Key Words: Herbig-Haro objects — ISM: individual objects (HH1/2) — ISM: jets and outflows — ISM: kinematics and dynamics — shock waves — stars: winds, outflows

1. INTRODUCTION

Wavelet transforms have many times been used as a tool for analyzing complex structures in the ISM. Wavelets have some advantages over traditional Fourier transform techniques in dealing with observational effects such as beam smoothing, noise, and edge artifacts (see. e.g. Stutzki et al 1998; Bensch et al. 2001). The fact that spatial localization is maintained in the transformed variables (as opposed to Fourier transforms, which replace spatial with wavenumber dimensions) allows studies of local effects in the turbulence, which include the so-

called “intermittency” and “local inverse cascades” (see, e.g., Meneveau 1991). Starting from the work of Gill & Henriksen (1990), wavelet techniques have been used to study both theoretical (e.g. Kowal & Lazarian 2010) and observational (e.g., Bensch et al. 2001; Arshakian & Ossenkopf 2016) turbulent astrophysical flows.

The study of observed astrophysical flows is mostly restricted to “snapshots” of the flow structures, because the evolutionary timescale of the flows is too long compared to human timescales. This is of course not the case in solar or interplanetary flows (with evolutions in short enough timescales), nor in laboratory flows. Astrophysical flows beyond the Solar System either evolve too slowly or, alternatively, are not angularly resolved, so that the time-evolution of their spatial structure is generally not

¹Instituto de Ciencias Nucleares, UNAM, México.

²Institute for Astronomy, Univ. of Hawaii, USA.

⁴DAFM, Univ. de las Américas, Puebla, México.

⁵Universitat Politècnica de Catalunya, Spain.

^{0†} Deceased.

known (other than through numerical modelling). Two exceptions are some young supernova remnants (see, e.g., the time-evolution of the SN 1987A shell described by Plait et al. 1995) and some Herbig-Haro outflows (see, e.g., Hartigan et al. 2011), which are angularly resolved and also show evolution on humanly attainable timescales.

In this paper, we calculate the wavelet spectra of four epochs (spanning ≈ 20 yrs) of H α and red [S II] HST images of the HH 1/2 region (these images are described in detail by Raga et al. 2016a, b). To these images, we apply an analysis which incorporates elements of previous studies made by us of the structures of HH objects (Riera et al. 2003) and (solar) coronal mass ejections (González-Gómez et al. 2010) using wavelets.

The interesting feature of the present study is the 20 yr time coverage of the four epochs of HST images. During this time, both HH 1 and 2 have shown major changes in their positions, morphologies and intensities (see Raga et al. 2016a, b, c). These images allow us to obtain the time evolution of the size distributions (through a wavelet analysis) of the clumpy emission of HH 1 and 2.

Even though very high Mach number HH objects might not correspond to truly turbulent flows, they do show complex, time-evolving knot structures. Our study addresses the question of whether or not the observed clumps are breaking up into smaller scale structures, as would be expected from a (forward) “turbulent cascade” process. Conversely, we could find that the emission knots are merging to form larger scale structures.

The paper is organized as follows. In § 2, we summarize the characteristics of the HST observations. In § 3, we show the spatial distributions of the characteristic sizes of the emitting structures of HH 1 and 2. In § 4, we present the time-evolving characteristic size distributions (corresponding to all of the emitting regions of HH 1 and 2). In § 5, the differences between the size distributions along and across the outflow axis are explored. The results are discussed in § 6. Finally, Appendix A describes the details of how the characteristic size distributions were obtained.

2. THE OBSERVATIONS

The characteristics of the four epochs of H α and red [S II] images which are available in the HST archive are summarized in Table 1. The 1994 images were described by Hester et al. (1998), the 1997 images by Bally et al. (2002), the 2007 images by

Hartigan et al. (2011) and the 2014 images by Raga et al. (2015a, b).

Figure 1 shows the 2014 H α and [S II] images, rotated 37° clockwise, so that the axis of the outflow is approximately parallel to the abscissa. The outflow source (seen at radio and IR wavelengths, see e.g. Rodríguez et al. 2000 and Noriega-Crespo & Raga 2012) is located in the central region of the frames.

In these rotated frames, we have defined domains around HH 1 and 2, which are shown with the white boxes in Figure 1. These domains are large enough so that the emission from HH 1 and 2 is always included within them, regardless of the substantial proper motions of the objects during the ≈ 20 years covered by the observations. In the rest of the paper, we discuss the properties of the emitting structures within these two domains. All of the frames used have a scale of $0''.1$ per pixel.

3. THE SPATIAL DISTRIBUTION OF THE CHARACTERISTIC SIZES

We convolved the four epochs of [S II] and H α images (see § 2 and Table 1) with “Mexican hat” wavelets of radii $\sigma = 1$ to 100 pixels (i.e., $0''.1$ to $10''$). For all of the pixels of position (x, y) with an emission flux larger than $I_c = 1.5 \times 10^{-15}$ erg s $^{-1}$ cm $^{-2}$ arcsec $^{-2}$ we computed the wavelet spectrum $S_{x,y}(\sigma)$ (i.e., the intensity of the pixel as a function of radius σ of the wavelets).

For these “pixels with detections” we searched through the spectra and found the characteristic sizes corresponding to local maxima of S vs. σ . These sizes of course correspond to the radii (not the diameters) of the emitting structures. Some of the spectra had peaks at the smallest wavelet size ($\sigma = 1$ pixel or $0''.1$, see above) and at most two other peaks at larger values of σ .

As discussed in Appendix A, pixels in the periphery of bright emitting knots have spectra with peaks at $\sigma = 1$ pixel (a result of the fact that they are in the “negative rings” around the bright knots). This appears to be the case in the maps of HH 1 and 2 (Figures 2 and 3), which show that the pixels with $0''.1$ peaks (in their wavelet spectra) systematically lie in the periphery of the emitting knots.

The spatial distributions of the first peak with $\sigma > 0''.1$ (see Figures 2 and 3) show that characteristic sizes of $\approx 0''.3$ are found at the positions of the HH 1 and 2 knots, and that sizes of up to $\approx 5''$ are found in the more diffuse emitting areas of these objects. The second peak (with $\sigma > 0''.1$) indicates characteristic sizes of $\approx 3'' \rightarrow 10''$, with the larger sizes (basically corresponding to the size of the full

TABLE 1
HST IMAGES OF THE HH 1/2 SYSTEM

Epoch	Filters	Emission Lines	Exposures [s]	Camera
1994.61	F656N	H α	3000	WFPC2
	F673N	[S II] 6716/6731	3000	WFPC2
1997.58	F656N	H α	2000	WFPC2
	F673N	[S II] 6716/6731	2200	WFPC2
2007.63	F656N	H α	2000	WFPC2
	F673N	[S II] 6716/6731	1800	WFPC2
2014.63	F656N	H α	2686	WFC3
	F673N	[S II] 6716/6731	2798	WFC3

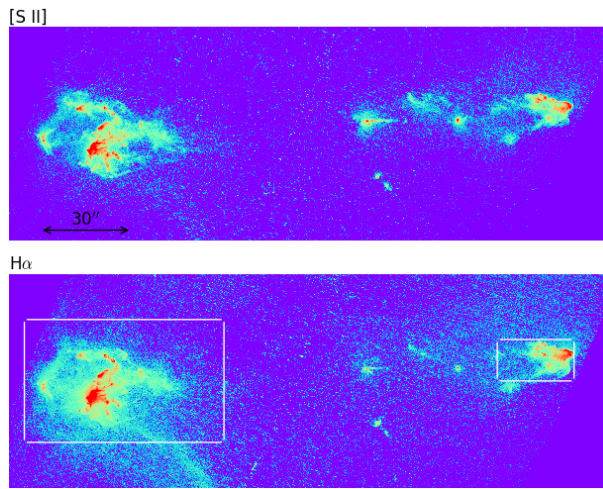


Fig. 1. HST images (taken in 2014) of the [S II] (top) and H α emission (bottom) of HH 1 and 2. The two frames (shown with a logarithmic color scale) have been rotated clockwise by 37°. The bottom frame shows the two boxes that we chose to isolate the HH 1 and 2 emission. The color figure can be viewed online.

emitting regions of the HH objects) located in the periphery of the HH 1 and 2 emission regions (see Figures 2 and 3).

4. THE CHARACTERISTIC SIZE DISTRIBUTION FUNCTIONS OF HH 1/2

4.1. General Description

Figures 4 and 5 show the characteristic size distributions of HH 1 and 2 (shown as the distribution $\sigma f(\sigma)$ as a function of $\log_{10} \sigma$) obtained from the four observed epochs in [S II] and H α . These size distributions have been computed in the way described in Appendix A. This Appendix also describes the general properties of the distributions.

In contrast to the wavelet spectra of individual pixels of HH 1 and 2, which have at most three peaks

as a function of σ (see § 3), the distributions of the characteristic sizes (obtained from all of the individual pixels) have 5-6 peaks. All size distributions have a peak at the smallest, $\sigma = 0''.1$ wavelet size. As discussed in § 3 and Appendix A, these peaks appear to be associated with the negative rings around the brighter knots, and we will not discuss them further.

The main, striking, characteristic of the size distributions is that they have a series of relatively well defined peaks, with similar separations in $\log_{10} \sigma$, corresponding to factors of $\approx 2 \rightarrow 3$ in the characteristic sizes of the successive peaks. The peaks indicating lower characteristic sizes have $\sigma \approx 0''.3 \rightarrow 0''.5$ (see Figures 4 and 5). Since these sizes correspond to the characteristic radii of the emitting structures,

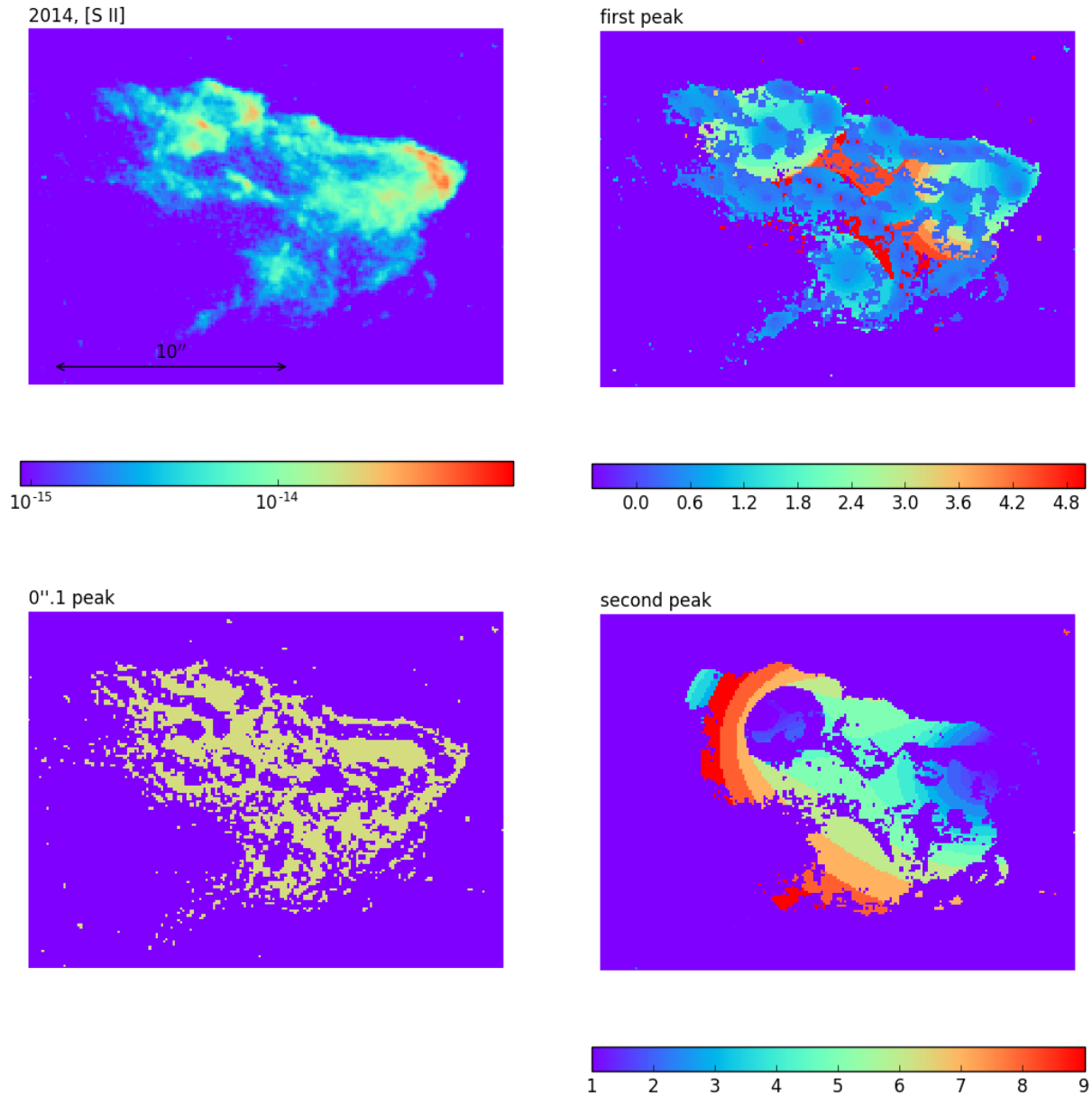


Fig. 2. Top left frame: the 2014 [S II] structure of HH 1 (shown with the logarithmic scale given in $\text{erg cm}^{-2}\text{s}^{-1} \text{arcsec}^{-2}$ by the bottom bar). Bottom left frame: the spatial distribution of the pixels that have a peak at the lowest ($\sigma = 0''.1$) wavelet size. Top right: spatial distribution of the first $\sigma > 0''.1$ peak of the wavelet spectra of the emitting pixels (the color scale shows the characteristic sizes, given in arcsec by the bottom bar, corresponding to the position of the first peak). Bottom right: the spatial distribution of the second peak in the wavelet spectra. The spectra of many of the emitting pixels do not show a second, $\sigma > 0''.1$ peak. The color figure can be viewed online.

it is clear that they are well resolved at the $0''.1$ resolution of the HST images.

The peaks indicating the largest characteristic sizes (see Figures 4 and 5) lie in the $4'' \rightarrow 9''$ range.

These sizes are similar to the size of the full emitting regions of HH 1 and 2.

When comparing the spectra obtained for the successive time frames, one sees that there are small shifts (mainly to larger characteristic sizes) of the lo-

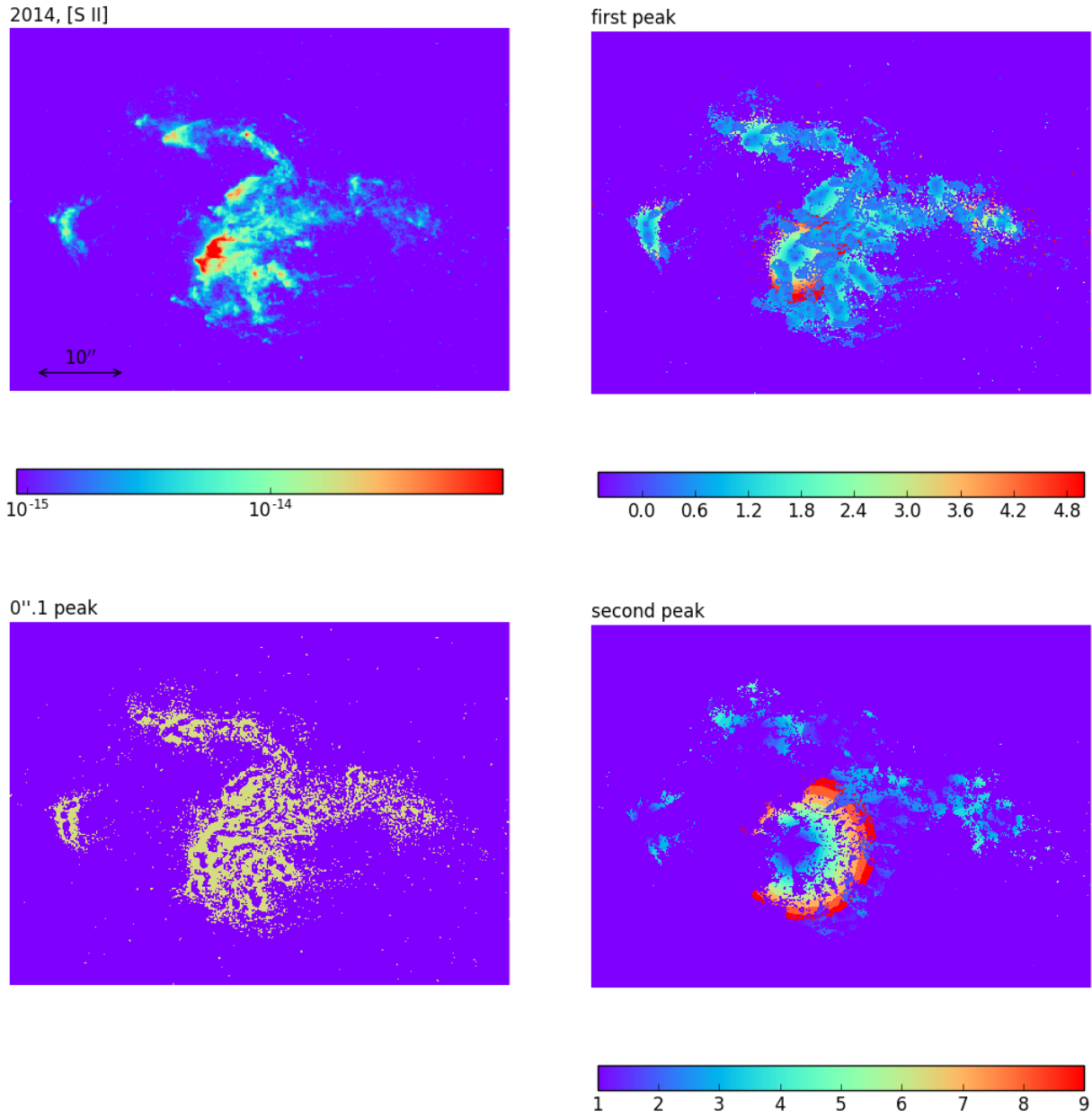


Fig. 3. The same as Figure 2, but for HH 2. The color figure can be viewed online.

cal maxima. This effect is discussed in more detail in the two following subsections.

4.2. [S II] characteristic sizes

Some of the features seen in the [S II] HH 1 size distributions (see Figure 4) are:

- a peak at $\sigma = 0''.4$ (indicated with the dashed, vertical line labeled a_{s1}) which shows up in the

1997 (and possibly also in the 1994) frame, but is absent in the 2007 and 2014 frames,

- a peak at $\sigma = 0''.7$ (vertical line labeled b_{s1}), visible in the size distributions of all frames,
- a peak at $\sigma = 1''.2$ (vertical line labeled c_{s1}), which is shifted to a somewhat larger, $\sigma \approx 1''.4$ size in the 2007 and 2014 frames,

- a “large size peak” at $\sigma = 4''$ (vertical line labeled d_{s1}) which becomes progressively shifted (with time) to larger sizes, up to $\sigma \approx 5''$ in the 2014 frame.

The [S II] HH 2 size distributions have:

- a broad structure centered around $\sigma = 0''.5$ (labeled a_{s2}), which is seen as a single peak only in the 2007 frame,
- a peak at $\sigma = 1''.4$ (labeled b_{s2}), which is not present in the 2014 frame,
- a peak at $\sigma = 3''$ (labeled c_{s2}), which becomes a strong feature in the 2014 frame,
- a “large size peak” at $\sigma \approx 6''.5$ (labeled d_{s2}), which is not seen as a peak in the 1994 frame, and migrates to larger sizes from 1997 to 2014.

4.3. H α Characteristic Sizes

Some of the features seen in the H α HH 1 size distributions (see Figure 4) are:

- a peak at $\sigma = 0''.3$ (labeled a_{h1}) which shows up in the 2007 and 2014 frames, but is absent in the 1994 and 1997 frames,
- a peak at $\sigma = 0''.7$ (labeled b_{h1}),
- a peak at $\sigma = 1''.2$ (labeled c_{h1}), which apparently migrates to a somewhat smaller, $\sigma = 1''$ size in the 2014 frame,
- a peak at $\sigma \approx 1''.8$ (labeled c'_{h1}), which migrates to somewhat larger sizes with increasing time, and becomes a dominant feature of the distribution in the 2014 frame,
- a “large size peak” at $\sigma \approx 6''$ (labeled d_{h1}).

The H α HH 2 size distributions have:

- a peak at $\sigma = 0''.4$ (labeled a_{h2}) only appearing in the 2014 frame,
- a peak at $\sigma = 0''.8$ (labeled b_{h2}), progressively migrating to somewhat larger sizes with time,
- a peak at $\sigma = 1''.5$ (labeled c_{h2}),
- a “large size peak” at $\sigma \approx 8''$ (labeled d_{h2} , also migrating to larger sizes.

5. 2D CHARACTERISTIC SIZE DISTRIBUTIONS

It is also possible to carry out a characterization of the emission structure of HH 1 and 2 using 2D, anisotropic wavelets. This is interesting because it is to be expected that an outflow may have different structures along and across the outflow axis.

We choose an elliptical “Mexican hat” wavelet kernel of the form:

$$g_{\sigma_x, \sigma_y}(x, y) = \frac{1}{\pi\sigma^2} \left[1 - \left(\frac{x}{\sigma_x} \right)^2 - \left(\frac{y}{\sigma_y} \right)^2 \right] e^{-(x/\sigma_x)^2 + (y/\sigma_y)^2}, \quad (1)$$

where σ_x and σ_y are the half-widths of the central peak along and across the outflow axis, respectively. A similar 2D version of the “Mexican hat” wavelet has been used by Riera et al. (2003) to study the characteristics of the HH 110 outflow.

We then convolve the 2014 H α images of HH 1 and 2 with 2D wavelets with σ_x and σ_y from 1 to 61 pixels ($0''.1$ to $6''.1$). In the resulting four-dimensional spectrum (with axes x , y , σ_x and σ_y), for all the spatial pixels (x, y) with H α intensities larger $I_c = 1.5 \times 10^{-15} \text{ erg s}^{-1} \text{ cm}^{-2} \text{ arcsec}^{-2}$ we compute the wavelet spectrum $S_{x,y}(\sigma_x, \sigma_y)$. For all these pixels we find the positions $(\sigma_x, \sigma_y)_m$ of the two peaks with smaller $\sigma = \sqrt{\sigma_x^2 + \sigma_y^2}$. Finally, we compute normalized 2D distribution functions $f_{2D}(\sigma_x, \sigma_y)$ of the determined peaks (using a 2D version of equation A6).

In Figure 6, we show the resulting 2D characteristic size distributions $\sigma_x \sigma_y f_{2D}(\sigma_x, \sigma_y)$ (corresponding to the $\sigma f(\sigma)$ 1D distributions shown in Figures 4 and 5) obtained from the 2014 H α maps of HH 1 and 2. Because of the relatively small number of emitting pixels within HH 1 and 2, these distributions are quite noisy. However, it is clear that a wide range of (σ_x, σ_y) combinations are present in different regions of HH 1 and 2, implying structures with sizeable elongations both along and across the outflow axis.

This calculation of $f_{2D}(\sigma_x, \sigma_y)$ characteristic size distributions is only meant as an illustration of the characteristics of a 2D analysis. A full analysis of this kind should include an application of arbitrary rotations ϕ to the image, after which the convolution with the elliptical wavelet g (see equation 1) should be made. We have not carried out such a study.

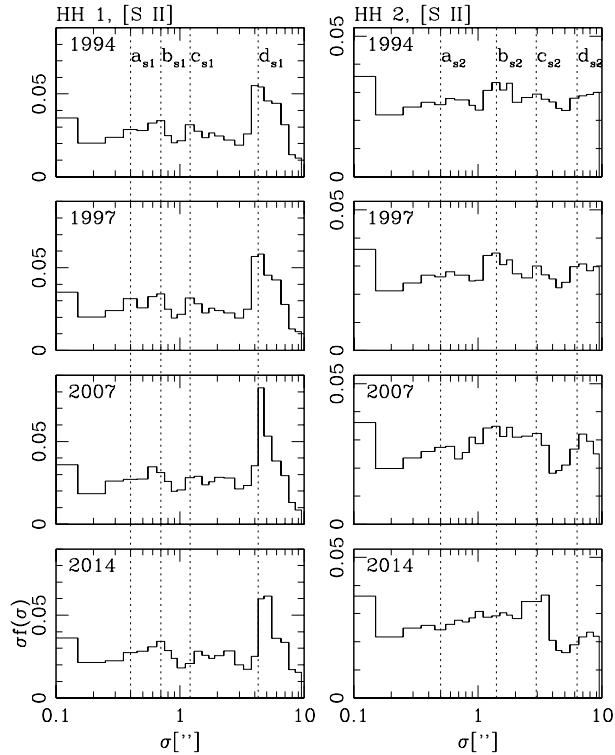


Fig. 4. Characteristic size distributions derived for the [S II] emitting regions of HH 1 (left) and HH 2 (right). The distributions obtained from the 1994 (top), 1997, 2007 and 2014 images (bottom) are shown.

6. CONCLUSIONS

We have computed the wavelet spectra of 4 epochs of H α and [S II] HST images of HH 1 and 2. The spectrum of each pixel (corresponding to the intensity as a function of radius σ of the wavelets) shows one, two or three maxima. The values of σ at which these maxima are found correspond to the characteristic sizes of emitting structures in the region around each pixel.

We first show maps of the characteristic sizes found for the [S II] emission of HH 1 and 2, observed in 2014 (see Figures 2 and 3). These maps show that the brighter knots of HH 1 and 2 are angularly resolved structures, with characteristic radii of $\approx 2 - 3''$. The fainter regions of these objects have characteristic sizes ranging from $3''$ up to $\approx 10''$ (i.e., similar to the full size of the HH 1 and 2 emission regions).

We then compute the distributions of the characteristic sizes found from the wavelet spectra of all of the emitting pixels in the HH 1 and HH 2 regions. These distributions show a number of peaks as a function of wavelet radius σ (Figures 4 and 5 showing the distributions obtained for the four epochs of [S II] and H α images, respectively). The distribu-

tions plotted as a function of $\log_{10} \sigma$ show a number of peaks, with spacings corresponding to factors of $\approx 2 - 3$ in the positions of the successive maxima. This result indicates that HH 1 and 2 have a hierarchy of structures with logarithmically spaced angular radii in the $0''.3 \rightarrow 10''$ range.

These peaks in the size distributions with spacings of factors $\approx 2 \rightarrow 3$ (see Figures 4 and 5) are a dominant feature of the knot size distributions of HH 1 and 2. However, their origin is unclear. The observed spacings between characteristic sizes could be:

- the result of an instability in the flow with a discrete set of dominating modes,
- the reflection of an ejection time-variability (from the outflow source) of appropriate characteristics,
- structures produced by a hierarchy of knot merging processes.

In all of these scenarios, line of sight superpositions of emitting structures will also have an important effect on the observed characteristic size spectra.

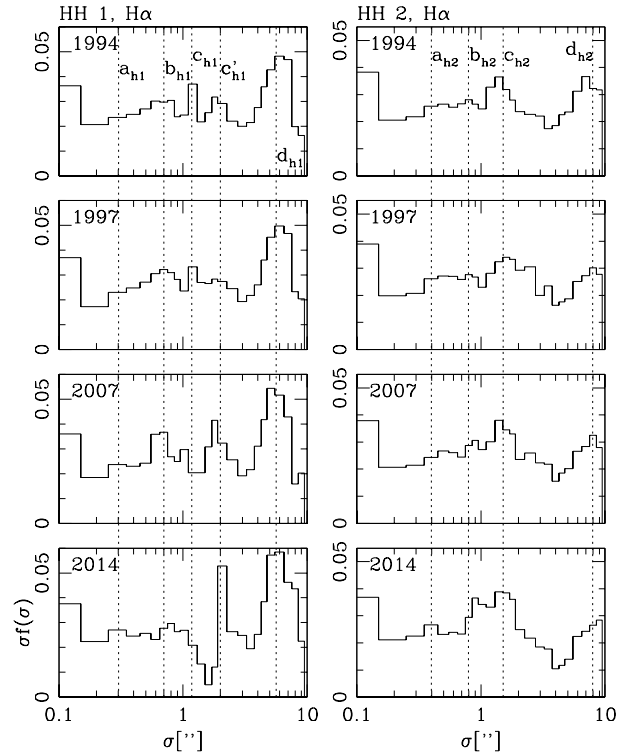


Fig. 5. Characteristic size distributions derived for the H α emitting regions of HH 1 (left) and HH 2 (right). The distributions obtained from the 1994 (top), 1997, 2007 and 2014 images (bottom) are shown.

We find that the [S II] and H α emissions (of both HH 1 and 2) have somewhat different size distributions (this can be seen comparing the corresponding columns of Figures 4 and 5). Different size distributions might be expected in structures formed by curved shocks, which have different [S II]/H α line ratios depending on the local normal shock velocity (as can be seen from predictions for plane-parallel, steady shocks such as the ones of Hartigan et al. 1987).

A comparison between the size distributions of the four indicators show that the relative height of the peaks changes with time, and that the positions of the peaks show small displacements. These displacements occur mostly towards larger characteristic radii of the emission structures.

This result clearly argues against the straightforward expectation of a turbulent cascade, in which large structures (eddies) break up into smaller scale structures. The expansion that we see at all scales could correspond to a general expansion of the HH objects, or to merging processes of the emitting knots.

Merging of smaller structures to form larger scale structures is predicted from solutions of Burgers's

equation (see Tatsumi & Kida 1972; Tatsumi & Tokunaga 1974; Raga 1992). As the solutions of Burgers's equation have strong resemblances to hypersonic flows, it is possible that we are seeing such an effect in HH 1 and 2. These HH objects have also been modeled numerically by Hansen et al. (2017) as a system of interacting clumps. This sort of “inverse cascade” would be an indication that we are not able to resolve the (forward) turbulent cascade at scales below the injection produced by the jet.

Even though we detect rather marginal displacements in the peaks of the size distribution functions (see § 4.2 and 4.3), it is evident that the shifts in the logarithms of the values of the peak positions are approximately scale independent. For example, for peak d_{s1} (located at $\sigma \approx 4''$, see Figure 4) we see a $\Delta\sigma_{20} \approx 1''$ over the 20 year time span of the HST images. This corresponds to a yearly expansion rate of $\Delta\sigma_1/\sigma \approx 0.01 \text{ yr}^{-1}$. Similar values of $\Delta\sigma/\sigma$ are found for all of the peaks with detected shifts. For the larger scales of HH 1/2 (of $\approx 10''$) these expansion rates correspond to a $\approx 200 \text{ km s}^{-1}$ velocity (similar to the dispersion of the proper motions of the HH 1/2 condensations, see Raga et al. 2016a, b), and for the smaller scales (of $\approx 3''$) the

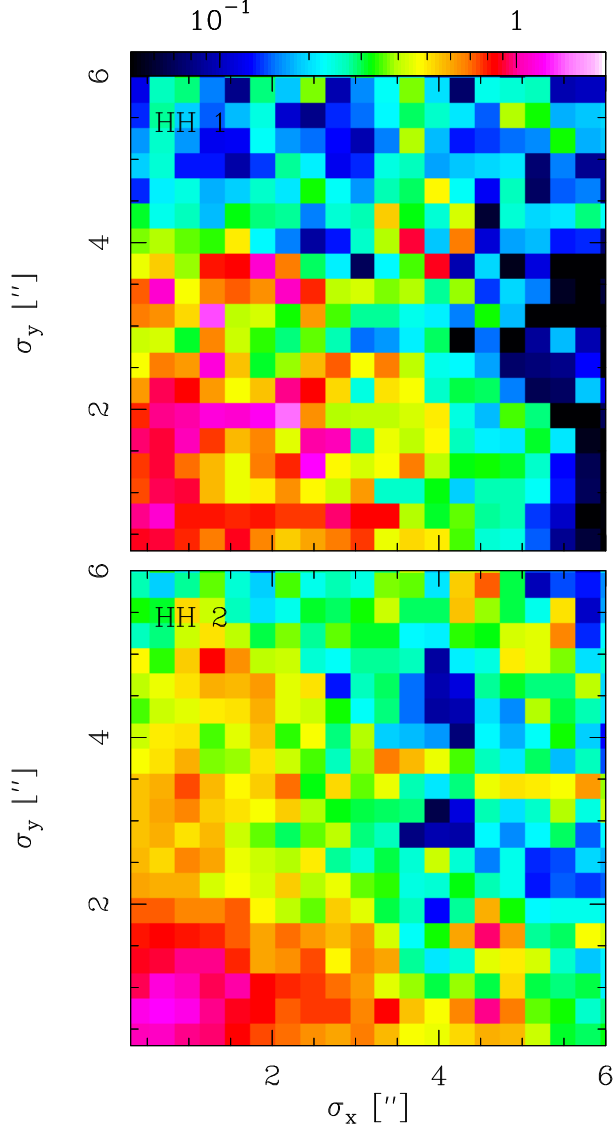


Fig. 6. 2D characteristic size distributions of the 2014 H α maps of HH 1 (top) and HH 2 (bottom). The axes of the two frames are the characteristic sizes σ_x (along) and σ_y (across the outflow axis), given in arcsec. The normalized distribution functions $\sigma_x \sigma_y f_{2D}(\sigma_x, \sigma_y)$ are shown with the logarithmic color scale given by the top bar. The color figure can be viewed online.

expansion velocity is $\approx 60 \text{ km s}^{-1}$ (assuming a distance of 400 pc to HH 1/2). These two velocities are highly supersonic at the temperature of $\approx 10^4 \text{ K}$ of the emitting regions of HH 1/2 (see Raga et al. 2016c).

If one assumes that the expansion that we observe at all scales is time-independent, one obtains a $\tau = \sigma / \Delta\sigma_1 \approx 100 \text{ yr}$ estimate for the time at which HH 1 and HH 2 had vanishing sizes. From this ar-

gument, one can conjecture that HH 1 and 2 were formed $\approx 100 \text{ yr}$ ago, at positions $\approx 15''$ closer the outflow source than the present positions of these two objects (for a proper motion of $\approx 300 \text{ km s}^{-1}$ for HH 1 and 2). This formation of HH 1 and 2 at large distances from the outflow source can easily be interpreted in terms of internal working surfaces formed by a variable velocity jet (see, e.g., Raga et al. 2015c and references therein).

Our present work is an effort to obtain a quantitative description of the time-evolution of the emission structures of HH 1 and 2. Though this can be done in different ways, we have focussed on obtaining wavelet spectra, and studying the size distributions that can be obtained from such an analysis. It will be interesting to apply this analysis to the structures of other HH objects, as well as to synthetic emission maps calculated from gasdynamical or MHD simulations of HH jets.

Support for this work was provided by NASA through grant HST-GO-13484 from the Space Telescope Science Institute. ARa acknowledges support from the CONACyT grants 167611 and 167625 and the DGAPA-UNAM grants IG100218, IA103315, IA103115, IG100516 and IN109715. ARi acknowledges support from the AYA2014+57369-C3-2-P grant. We thank an anonymous referee for comments which led to the calculations presented in § 5. We are most sad to say that Angels Riera died in September 2017. We regret the loss of our close friend and collaborator.

APPENDIX

A. FINDING CHARACTERISTIC SIZES FROM WAVELET SPECTRA

We start from an image, defined as an intensity $I(x, y)$ over a 2D, Cartesian (x, y) domain. Convolved maps I_σ are calculated through the integral

$$I_\sigma(x, y) = \int \int I(x', y') g_\sigma(x-x', y-y') dx' dy', \quad (\text{A2})$$

where $I(x', y')$ is the original (i.e., not convolved) image, and (x, y) are the coordinates of the convolved image. The convolutions are carried out with a standard, “Fast Fourier Transform” method.

In equation (A2), g_σ is the “wavelet kernel” for which we have chosen the “Mexican hat” function

$$g_\sigma(x, y) = \frac{1}{\pi\sigma^2} \left(1 - \frac{x^2 + y^2}{\sigma^2} \right) e^{-(x^2 + y^2)/\sigma^2}, \quad (\text{A3})$$

where σ is the half-width of the central peak.

Now, following e.g. Gill & Henriksen (1990), we define the (normalized) spatially integrated wavelet spectrum

$$S_{tot}(\sigma) = \frac{\int \int \max[I_\sigma(x, y), 0] dx dy}{\int \int \int \max[I_\sigma(x, y), 0] dx dy d\sigma}. \quad (\text{A4})$$

Also, we define the normalized wavelet spectrum at an arbitrary point (x_a, y_a) as

$$S_a(\sigma) = \frac{I_\sigma(x_a, y_a)}{\int I_\sigma(x_a, y_a) d\sigma}. \quad (\text{A5})$$

The integrals in equations (A4) and (A5) are carried out over the full chosen ranges of x , y and σ .

In order to illustrate the behavior of these spectra, we use a simple “test image”. We generate this image in the following way:

- we define a 500×500 pixel image, to which we assign a $0''.1$ per pixel angular size (i.e., the pixel size of the HST images);
- on a zero intensity background, we add the intensities of two populations of circular “spots”: a first population with a radius of $r_1 = 1''$ and a (dimensionless) intensity $I_1 = 3$, and a second population with $r_2 = 5''$ and $I_2 = 1$;
- the central points of the circular spots are randomly chosen, and 90% of these points are randomly assigned “first population” spots (the remaining 10% being assigned the larger, “second population” spots);
- a total number of 100 spots is introduced in this way, resulting in a map with circular spots of the two chosen fluxes/radii, and regions of higher flux in which two or more spots are superposed.

The resulting image is shown in Figure 7.

We now convolve the test image with Mexican hat wavelets (see equation A3) of widths $\sigma = 1, 2, 3, 4, 5, 6, 7, 8, 9, 10, 12, 14, 16, 18, 20, 25, 30, 35, 40, 45, 50, 60, 70, 80, 90$ and 100 pixels (which one has to multiply by 0.1 to obtain the widths in arcseconds). From the convolved images $I_\sigma(x, y)$ we calculate the spatially integrated spectrum (see equation A4) and the spectra at the three locations A, B and C indicated in Figure 7.

The four resulting spatial spectra are shown in Figure 8. From this figure, we see that

- the spatially integrated spectrum $S_{tot}(\sigma)$ (top frame) shows a peak at a radius of $\approx 1''$, corresponding to the small, bright spots (of the first

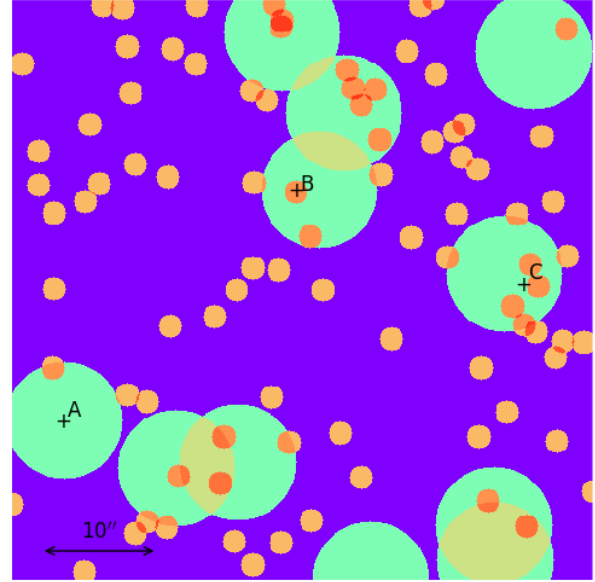


Fig. 7. Test image with a random distribution of two knot populations. The generation of this image is described in Appendix A. The positions of 3 chosen pixels are shown (and labeled A, B and C). The wavelet spectra at these positions are shown in Figure 8.

population of spots, see above). The population of faint, large spots does not produce a maximum in S_{tot} , but instead coincides with an inflection point in the spectrum (seen at $\sigma \approx 5''$ in the plot). This possible appearance of characteristic sizes as inflection points in the spatially integrated wavelet spectra has been discussed by González-Gómez et al. (2010);

- the spectrum at point A (see Figure 7 and the second frame of Figure 8) shows a peak at the approximate size of the “large knot” population;
- the spectrum at point B shows a peak at the size of the “small knot” population;
- the spectrum at point C shows a negative valley for $\sigma < 1''$ and a peak at the size of the “large knot” population.

From this analysis we see that while the spectra at individual points show maxima at the known sizes of the chosen “emission spots”, the “large spot” feature does not appear as a maximum in the spatially integrated spectrum. We also see that the maxima in the spectra at individual points do not have the same positions as the radii of our spots ($r_1 = 1''$ and $r_2 = 5''$, see above). For the two knot populations, the maxima (in the wavelet spectra) are located at

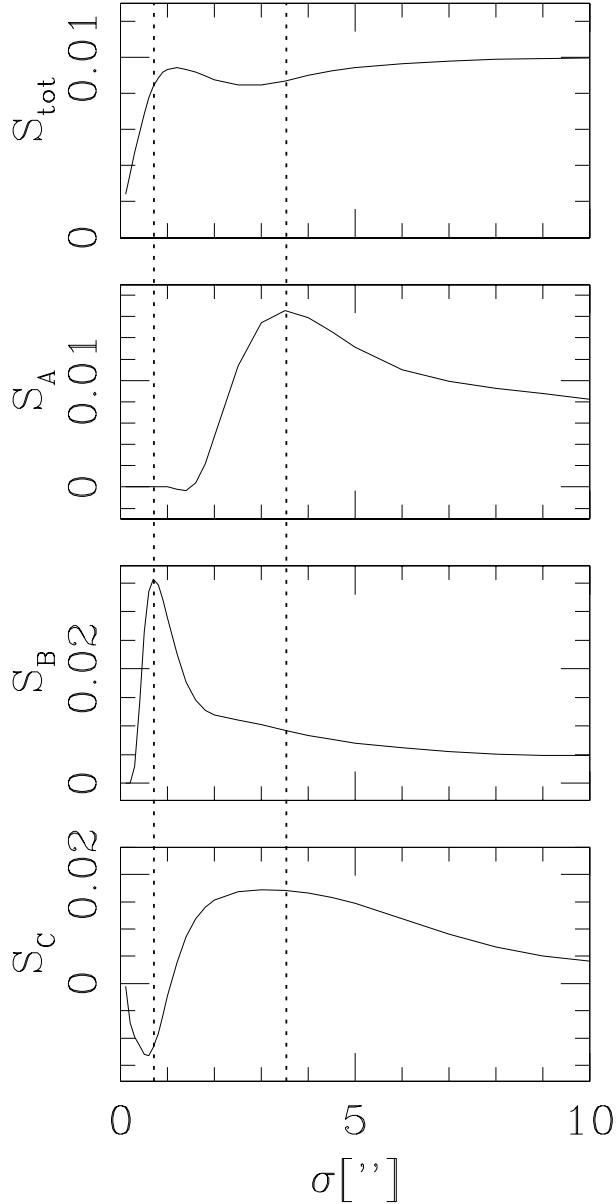


Fig. 8. Wavelet spectrum S_{tot} integrated over all pixels with positive spectral values (top) and wavelet spectra S_A , S_B and S_C at the positions of pixels A, B and C of Figure 7 (three bottom frames). The spectra are given as a function of the radius σ (in arcsec) of the wavelets. The two dashed, vertical lines indicate the values of the root-mean square radii of the two knot populations of our synthetic image.

characteristic sizes $\sigma_{1,2} \approx r_{1,2}/\sqrt{2}$, corresponding to the root mean square radii of the (flat) intensity distributions within the emission spots. The two root-mean-square radii (of the knot populations) are shown with the vertical, dotted lines in Figure 8.

An interesting effect is seen in the wavelet spectrum of point C (see Figure 7), shown in the bottom frame of Figure 8: for points in the vicinity of bright emission features, at small σ values one obtains a (negative) minimum in $S(\sigma)$. This is a direct result of the fact that bright features produce a ring of “negative intensities” in the convolved maps (see equation A2). In this way, a peak is produced at the smallest σ value (of 1 pixel, in our case corresponding to $0''.1$) of the computed spectrum.

Therefore, peaks in the spectrum at the smallest σ value can be a result of the proximity to a bright feature. Alternatively, such a peak could also indicate the presence of an unresolved emission structure (at the point at which we are calculating the spectrum), or it could be a result of noise in the image. Because of this uncertainty in the meaning of peaks at $\sigma = 1$ pixel sizes in the wavelet spectra, in the analysis of the HH 1/2 images we consider them independently from the peaks found at other σ values (basically, we show their spatial distribution, but otherwise disregard them).

Because of the fact that the spatially integrated wavelet spectrum does not preserve the peaks seen in the spectra of individual points (indicating characteristic sizes of the emission features), we proceed as follows:

- we first compute the wavelet spectra at all points (x_a, y_a) with intensities $I(x_a, y_a) > I_c$, where I_c is a low intensity cutoff,
- we then find all of the σ_m values at which the $S_a(\sigma)$ have maxima (including the ones at $\sigma = 1$ pixel), for all of the chosen points,
- with these σ_m values, we construct a distribution function of characteristic sizes of the emitting structures of the image.

Once the values of σ_m have been calculated (these are the values of σ for which the spectra of all of the bright enough pixels have maxima as a function of σ), we calculate a binned distribution function as:

$$f(\sigma_l) = \frac{N(\sigma_l)}{A\Delta\sigma_l}, \quad (\text{A6})$$

where σ_l is one of the σ -values of our discrete wavelet spectrum, $N(\sigma_l)$ is the number of pixels whose spectra have maxima at σ_l , $\Delta\sigma_l$ is the width of the interval in σ represented by σ_l (computed with the neighboring values of the σ discretization) and A is a normalization constant chosen so that $\int f(\sigma) d\sigma = 1$.

Figure 9 shows the logarithmic characteristic size distribution $\sigma f(\sigma)$ computed from the image shown

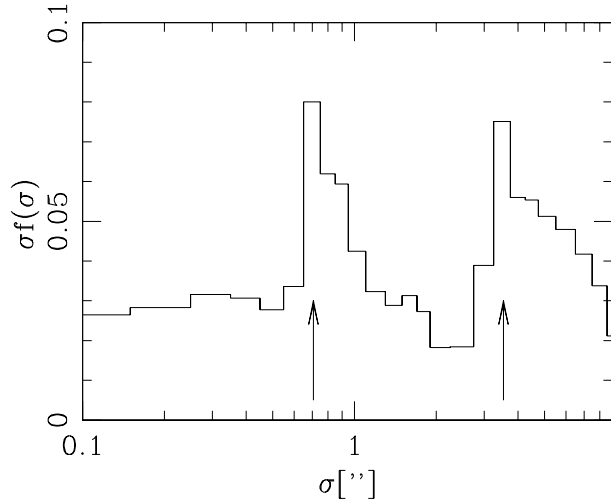


Fig. 9. Distribution function $f(\sigma)$ (see equation A6) of the positions of the peaks in the spectra of all emitting pixels. Actually, we plot $\sigma f(\sigma)$, which is the distribution of $\log_{10} \sigma$. The two arrows indicate the values of the root-mean square radii of the two knot populations of our synthetic image.

in Figure 7. To calculate this size distribution we have chosen a cutoff intensity $I_c = 0$ (see above). The size distribution (of the maxima of the wavelet spectra of the chosen points in the image) has two peaks at the positions of the root mean square radii of the two populations of emission spots (these sizes are indicated with the vertical arrows in Figure 9).

The two peaks of the distribution (see Figure 9) are located at $\sigma_1 \approx 0.7''$ and $\sigma_2 \approx 3.2''$ (see Figure 9). The heights $\sigma_1 f_1 = 0.080$ and $\sigma_2 f_2 = 0.075$ of the peaks are proportional to the number of pixels of the image within emitting structures of sizes σ_1 and σ_2 , respectively. The relative numbers of emitting knots N_1 and N_2 with these two characteristic sizes (and within bins of equal logarithmic width) can be estimated by noting that the central peaks of the corresponding wavelets (see equation A3) have $\pi\sigma_{1,2}^2$ pixels. Therefore, the ratio of the numbers of knots in the two peaks is $N_1/N_2 \approx (f_1/f_2)(\sigma_2/\sigma_1) = 20.9$. This number has to be compared with the ratio of the numbers of knots of the two sizes introduced in the simulated image (see above), which has a value of ≈ 10 .

It is clear that it is easier to determine the characteristic sizes of the emitting structures from the size distribution function $\sigma f(\sigma)$ (Figure 9) than from the

much smoother, spatially integrated wavelet spectrum (top frame of Figure 8). Because of this, in the present paper we analyze the size distributions of the images of HH 1 and 2 in order to determine the evolution of the characteristic sizes of their emitting structures.

REFERENCES

- Arshakian, T. G. & Ossenkopf, V. 2016, *A&A*, 585, 98
 Bally, J., Heathcote, S., Reipurth, B., et al. 2002, *AJ*, 123, 2627
 Bensch, F., Stutski, J., & Ossenkopf, V. 2001, *A&A*, 366, 636
 Gill, A. G. & Henriksen, R. N. 1990, *ApJ*, 365, L27
 González-Gómez, D. I., Blanco-Cano, X., & Raga, A. C. 2010, *SoPh*, 266, 337
 Hansen, E. C., Frank, A., Hartigan, P., & Lebedev, S. V. 2017, *ApJ*, 837, 143
 Hartigan, P., Raymond, J. C., & Hartmann, L. W. 1987, *ApJ*, 316, 323
 Hartigan, P., Foster, J. M., Wilde, B. H., et al. 2011, *ApJ*, 736, 29
 Hester, J. J., Stapelfeldt, K. R., & Scowen, P. A. 1998, *AJ*, 116, 372
 Kowal, G. & Lazarian, A. 2010, *ApJ*, 720, 742
 Meneveau, C. 1991, *PhRvL*, 66, 1450
 Noriega-Crespo, A. & Raga, A. C. 2012, *ApJ*, 750, 101
 Plait, P. C., Lundqvist, P., Chevalier, R. A., & Kirshner, R. P. 1995, *ApJ*, 439, 730
 Raga, A. C. 1992, *MNRAS*, 258, 301
 Raga, A. C., Reipurth, B., Esquivel, A., & Bally, J. 2016a, *AJ*, 151, 113
 Raga, A. C., Reipurth, B., Velázquez, P. F., Esquivel, A., & Bally, J. 2016b, *AJ*, 152, 186
 Raga, A. C., Reipurth, B., Castellanos-Ramírez, A., & Bally, J. 2016c, *RMxAA*, 52, 347
 Raga, A. C., Reipurth, B., Castellanos-Ramírez, A., Chiang, Hsin-Fang, & Bally, J. 2015a, *AJ*, 150, 105
 ———. 2015b, *ApJ*, 798, L1
 Raga, A. C., Rodríguez-Ramírez, J. C., Cantó, J., & Velázquez, P. F. 2015c, *MNRAS*, 454, 412
 Riera, A., Raga, A. C., Reipurth, B., et al. 2003, *AJ*, 126, 327
 Rodríguez, L. F., Delgado-Arellano, V. G., Gómez, Y., et al. 2000, *AJ*, 119, 882
 Stutzki, J., Bensch, F., Heithausen, A., Ossenkopf, V., & Zielinsky, M. 1998, *A&A*, 336, 697
 Tatsumi, T. & Kida, S. 1972, *JFM*, 55, 659
 Tatsumi, T. & Tokunaga, H. 1974, *JFM*, 65, 581

- A. Esquivel and A. C. Raga: Instituto de Ciencias Nucleares, Universidad Nacional Autónoma de México, Ap. 70-543, 04510, Ciudad de México, México (raga@nucleares.unam.mx).
- D. González-Gómez: DAFM, UDLAP, Ex Hda. Sta. Catarina Mártir, C:P. 72810, Puebla, México.
- B. Reipurth: Institute for Astronomy, University of Hawaii at Manoa, Hilo, HI 96720, USA.
- A. Riera: Departament de Física i Enginyeria Nuclear, EUETIB, Universitat Politècnica de Catalunya, Comte d'Urgell 187, E-08036 Barcelona, España.